Received: 27 January 2024 | Revised: 21 May 2024 | Accepted: 28 May 2024

DOI: 10.1002/sus2.220

RESEARCH ARTICLE

SusMat WILEY

Sulfone-functionalized stable molecular single crystals for photocatalytic hydrogen evolution

Xunliang Hu[1] | Xiaoju Yang[1] | Bingyi Song[1] | Zhen Zhan[1,2] | Ruixue Sun[1] | Yantong Guo[1] | Li-Ming Yang[1] | Xuan Yang[1] | Chun Zhang[3] | Irshad Hussain[4] | Xiaoyan Wang[1] | Bien Tan[1]

[1]Key Laboratory of Material Chemistry for Energy Conversion and Storage Ministry of Education, Hubei Key Laboratory of Material Chemistry and Service Failure, School of Chemistry and Chemical Engineering, Huazhong University of Science and Technology, Wuhan, China

[2]Department of Applied Physics, The Hong Kong Polytechnic University, Kowloon, Hong Kong, China

[3]College of Life Science & Technology, Huazhong University of Science and Technology, Wuhan, China

[4]Department of Chemistry and Chemical Engineering, SBA School of Science and Engineering, Lahore University of Management Sciences, Lahore, Pakistan

Correspondence
Xiaoyan Wang and Bien Tan, Key Laboratory of Material Chemistry for Energy Conversion and Storage Ministry of Education, Hubei Key Laboratory of Material Chemistry and Service Failure, School of Chemistry and Chemical Engineering, Huazhong University of Science and Technology, Luoyu Road No. 1037, 430074 Wuhan, China.
Email: xiaoyan_wang@hust.edu.cn; bien.tan@mail.hust.edu.cn

Funding information
International S&T Cooperation Program of China, Grant/Award Numbers: 2018YFE0117300, 22161142005; Natural Science Foundation of Hubei Province, Grant/Award Number: 2022CFB720; Huazhong University of Science and Technology (HUST) Academic Frontier Youth Team, Grant/Award Number: 2019QYTD11; HUST, Grant/Award Numbers: 2006013118, 3004013105; Fundamental Research Funds for the Central Universities, Grant/Award Number: 2019kfyRCPY116; Innovation and Talent Recruitment Base of New Energy Chemistry and Device,

Abstract

Highly crystalline organic semiconductors are ideal materials for photocatalytic hydrogen evolution in water splitting. However, the instability and complex synthesis processes of most reported organic molecule-based photocatalysts restrict their applications. In this study, we introduce benzo [1,2-b:4,5-b′] bis [1] benzothiophene-3,9-dicarboxylic acid, 5,5,11,11-tetraoxide (FSOCA), a highly crystalline, stable molecular crystal that is easy to synthesize and serves as an efficient photocatalyst for the hydrogen evolution reaction. FSOCA exhibits high efficiency in sacrificial hydrogen evolution reaction (760 μmol h^{-1}, 76 mmol g^{-1} h^{-1} at 330 mW cm^{-2}; 570 μmol h^{-1}, 57 mmol g^{-1} h^{-1} at 250 mW cm^{-2}), and FSOCA remains stable during photocatalysis for up to 400 h. Experiments and theoretical studies confirmed the presence of hydrogen bonds between the sulfone group and the sacrificial agent (ascorbic acid). This interaction significantly improved the oxidation reaction kinetics and boosted the photocatalytic performance. This study presents a scalable and convenient approach to synthesize highly crystalline, active, and stable organic photocatalysts with potential applications in large-scale photocatalysis.

KEYWORDS
exceptional durability, molecular single crystals, photocatalytic water splitting

Grant/Award Number: B21003; National Natural Science Foundation of China, Grant/Award Numbers: 21975086, 22305087, 52203259, 21873032, 22073033, 21673087, 21903032

1 | INTRODUCTION

Photocatalytic water splitting to produce green hydrogen is considered an ideal technology.[1,2] Organic photocatalysts, made from earth-abundant elements such as carbon and nitrogen, can be synthetically tuned to absorb visible light while maintaining appropriate energy levels for various photocatalytic reactions.[3–8] A wide array of organic semiconductors, especially polymer-based materials, have been developed for photocatalytic hydrogen evolution reactions (HERs), for example, g-C_3N_4,[1,9–13] linear conjugated polymers,[14,15] conjugated microporous polymers,[16–18] covalent organic frameworks,[19–21] and covalent triazine-based frameworks.[22–25] However, it is difficult for most of above-mentioned polymeric materials to obtain highly crystalline structure. Abundant defects exist in these organic semiconductors, which are prone to the recombination of excitons, significantly limiting their photocatalytic performance.[23,26–29] Moreover, the synthesis of many of these polymeric materials entails complexity or relies on expensive monomers. Hence, there exists a pronounced yet unfulfilled demand for readily synthesized and highly crystalline organic photocatalysts with low exciton recombination efficiency and high performance.

Organic molecular semiconductors are typically readily accessible in highly crystalline structures via solution-processed technology. Their highly crystalline structure can efficiently promote the exciton diffusion and inhibit recombination.[30,31] Till now, Y6's derivatives,[31] perylenediimide,[32–35] porphyrin,[36–38] and carbazole[39,40] have been reported as promising photocatalysts for HER applications. Stupp and coworkers have conducted pioneering research on molecular semiconductors based on perylenediimide, the perylene monoimide chromophore amphiphile demonstrating a photocatalytic hydrogen evolution rate of 6.56 μL h^{-1}.[32] Recently, a crystalline perylenetetracarboxylic acid nanosheet-based materials exhibited a high hydrogen evolution rate of 118.9 mmol g^{-1} h^{-1}.[3] Although crystalline structure has endowed organic molecular semiconductors with good exciton diffusion ability, the development of organic molecular semiconductors is still limited due to their complex synthesis processes and instability. For instance, the synthesis of carbazole derivatives[39,40] as well as Y6 derivatives[31] is too complicated and need expensive monomers, resulting in moderate to good performance. Moreover, most molecular semiconductors are less stable in photocatalysis process, which limited their practical application. Cooper and coworker reported that the crystallinity and activity of a pyrene-based organic semiconductor would both experience a notable decrease following a 6-h photocatalytic experiment.[29] In summary, while the crystalline structure renders molecular semiconductors attractive materials for the photocatalytic HER, there remains plenty of room for enhancement, for example, enhanced photocatalytic activity, easier synthesis, and improved stability.

The instability of organic molecule-based semiconductors arises from oxidative degradation of their oxidized forms. It has been confirmed that the oxidative stability of organic molecules can be enhanced via removing functional groups and increasing the oxidation potential (much deeper highest occupied molecular orbital [HOMO] energy). The improved oxidative stability is achieved by the fast transfer of holes to water or sacrificial agent molecules to avoid the oxidative degradation of organic molecules.[41] Inspired by this, we present herein a stable molecule photocatalyst (benzo [1,2-b:4,5-b′] bis [1] benzothiophene-3,9-dicarboxylic acid, 5,5,11,11-tetraoxide [FSOCA]) for the HER. Our hypothesis posits that the electron-withdrawing group $–SO_2$ can lower the energy of the HOMO and that the atoms of FSOCA have already reached their highest valence state, which endow FSOCA with good oxidative stability. Moreover, the sulfone groups serve as a "lock" for the flipped aromatic rings, substantially enhancing the delocalized range and rigidity of the skeleton as well as the interlayer π–π interaction. Strong π–π interactions and hydrogen bonding between carboxyl groups facilitate the attainment of a highly crystalline structure. Additionally, increased delocalization leads to reduced spatial overlap between electron and hole wavefunctions, resulting in lower exciton binding energy (E_b), thereby enhancing the charge transfer process.[42] The aforementioned factors contribute to FSOCA exhibiting a highly crystalline structure with low exciton binding energy, consequently leading to excellent photocatalytic performance. Significantly, FSOCA exhibits remarkable stability and achieves high performance in the HER during prolonged photocatalytic processes (up to 400 h). Its HER activity is up to 76 mmol g^{-1} h^{-1} at 330 mW cm^{-2} (570 μmol h^{-1}, 57 mmol g^{-1} h^{-1} at 250 mW cm^{-2}),

resulting in one of the most outstanding performances among organic photocatalysts. Furthermore, FSOCA can be synthesized easily on a laboratory scale, up to tens of grams. This study presents a promising approach for developing organic semiconductor-based photocatalysts with high HER performance, excellent stability, and ease of synthesis.

2 | RESULTS AND DISCUSSION

2.1 | Chemical structure of FSOCA, SOCA, and TPCA

FSOCA was prepared through the sulfonation reaction of [p-terphenyl]−4,4″-dicarboxylic acid (TPCA), which exhibits insolubility in most common organic solvents and water but shows slight solubility in dimethyl sulfoxide (DMSO) and N-methylpyrrolidone (NMP). A control sample (5,5-dioxo-5H-dibenzo[b,d]thiophene-3,7-dicarboxylic acid [SOCA]) with one sulfone group was purchased commercially. Their structures were analyzed by nuclear magnetic resonance spectroscopy and/or single-crystal X-ray crystallography (SCXRD). The proton nuclear magnetic resonance (^{1}H NMR) spectrum of FSOCA (Figure S1) showed three peaks at 8.94 ppm (2H, s), 8.31 ppm (2H, d), and 8.21–8.23 ppm (4H, t), which correspond to the four different types of protons in FSOCA. The ^{13}C NMR spectrum of FSOCA (Figure S2) exhibited nine peaks within the range of 118–167 ppm. The peak observed at 167 ppm corresponds to the carbon of the carbonyl group, while the peaks falling within the range of 118–143 ppm can be attributed to the aromatic carbon. ^{1}H NMR spectrum of TPCA (Figure S3) showed two peaks at 8.03 ppm (4H, d) and 7.88 ppm (8H, d). ^{1}H NMR spectrum of SOCA (Figure S4) showed three peaks at 8.53 ppm (2H, d), 8.50 ppm (2H, s), and 8.46 ppm (2H, d). Large crystals of FSOCA- and SOCA-containing solvent were obtained and characterized by SCXRD, while TPCA had yet to obtain the crystals. The structure of FSOCA•NMP was refined (CCDC no. 2287846, Figure S5), providing clear evidence of the chemical structure of FSOCA. Additionally, the chemical structure of SOCA was definitively confirmed through the refinement of SOCA•DMF (CCDC no. 2251963, Figure S6). Fourier transform infrared (FTIR) spectrum (Figures S7–S9) showed strong peak of carbonyl group (–C═O) at about 1700 cm^{-1}. X-ray photoelectron spectroscopy analysis revealed the presence of C, O, and S elements in FSOCA. The peaks at 169.2 and 168.0 eV in S2p spectrum were assigned to S in –SO_2 groups. The peak at 288.9 eV in C1s spectra can be assigned to carbonyl group, and 284.9 eV is assigned to aromatic carbon. The peaks at 532.6 and 531.9 eV in O1s spectra can be assigned to oxygen atoms in –COOH and –SO_2 groups, respectively (Figure S10). Thermogravimetric analysis showed good thermal stability (>300°C) of FSOCA, SOCA, and TPCA (Figure S11). The nitrogen adsorption–desorption curve (Figure S12a) revealed the presence of both micropore and macropore in FSOCA. Micropores are likely a result of specific crystal defects, while macropores may formed due to particle aggregation. Additionally, the calculated Brunauer-Emmett-Teller (BET) surface of FSOCA is about 82 m^2 g^{-1}. Pore size distributions were calculated using the Barret-Joyner-Halenda (BJH) method (Figure S12b), revealing microporous structures located at approximately 2 nm.

2.2 | Crystal structures of FSOCA and SOCA without solvent

After elucidating their chemical structures, we further analyzed the crystal structures of FSOCA and SOCA in their solvent-free states. First, powder X-ray diffraction (PXRD) revealed that both FSOCA (Figure 1(B)) and SOCA (Figure S14) exhibited exceptionally high crystallinity. As shown in Figure 1(B), the peaks near 6.97°, 12.06°, 14.01°, 18.06°, and 25.04° were assigned to (001), (010), (112), ($\bar{1}$22), and (102) crystallographic planes, respectively. FSOCA maintains high degree of order after various solvent treatments, indicating good stability of the crystal. The slight reduction in the grain size of FSOCA may be attributed to solvent-induced crystal exfoliation (Figure S13). However, TPCA exhibits a low degree of ordered structure (Figure S15), and only three peaks in PXRD curves show that they are likely originating from self-assembled structures. The crystalline structure was further analyzed using microcrystal electron diffraction (MicroED). From the reconstructed 3D lattice in reciprocal space, the lattice constants of FSOCA (Figure 1(C–E)) were determined as follows: a = 5.06 Å, b = 7.63 Å, c = 12.97 Å, α = 89.07°, β = 100.93°, and γ = 101.94°, with a volume of V = 480.9 Å^3, which was identified to P$\bar{1}$ (no. 2) space group. Within a unit cell, FSOCA molecules are interconnected via hydrogen bonding (Figures 1(D,E) and S16), the hydrogen bond length is 2.64 Å. The lattice constants of SOCA were determined as follows: a = 19.27 Å, b = 14.31 Å, c = 5.03 Å, α = 90.00°, β = 92.48°, and γ = 90.00°, with volume of V = 1385.7 Å^3 (Figure S17), corresponding to space group P21 (no. 4). Within a unit cell, nine SOCA molecules were linked via hydrogen bonding between two carboxyl groups (Figures S18 and S19).

FSOCAs tend to adopt a rod-shaped, layered structure (Figures S20 and S21). Similarly, an SOCA exhibits a nanorod-type structure (Figure S22). In contrast, TPCA presents as irregular nanosheets (Figure S23).

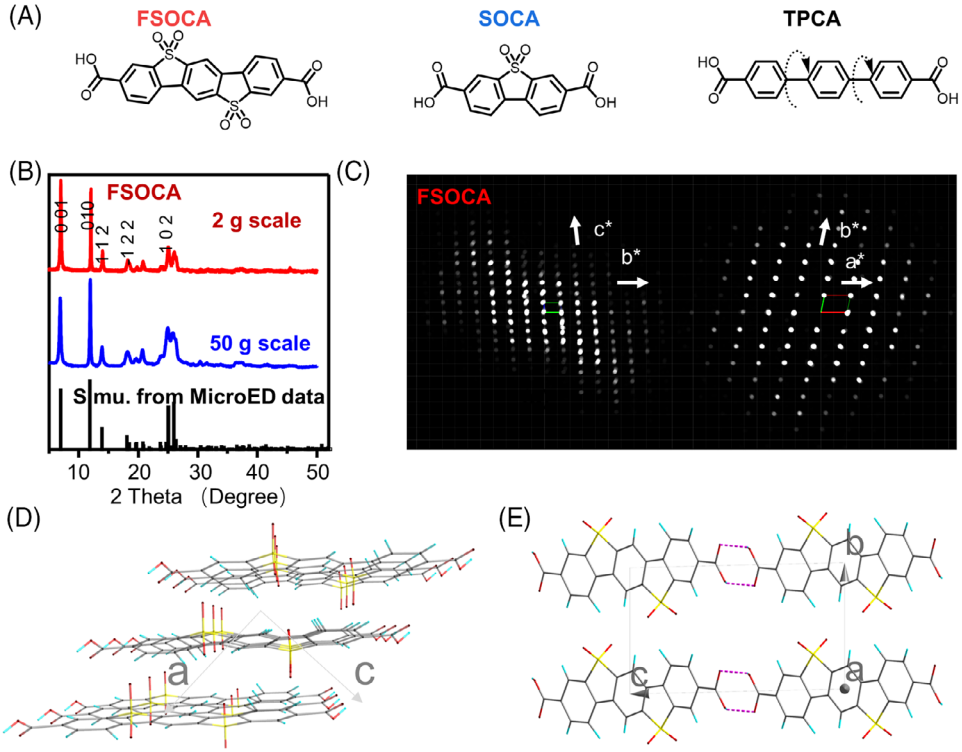

FIGURE 1 (A) Molecular structures of three aromatic carboxylic acids. (B) Experimental powder X-ray diffraction (PXRD) data for benzo [1,2-b:4,5-b′] bis [1] benzothiophene-3,9-dicarboxylic acid, 5,5,11,11-tetraoxide (FSOCA) from different synthesis scales (2 and 50 g) and simulated PXRD data based on the crystal structure solved via cryo-electron diffraction tomography (EDT). (C) EDT data projected along the [100], [001] direction for the FSOCA with routine holder and with cryo-holder. (D) Supercell structure of FSOCA viewed via *b*-axis. (E) Supercell structure of FSOCA viewed via *a*-axis.

Interestingly, FSOCA's morphology appears to be influenced by the solvent used (Figures S24–S26), possibly due to the exfoliation in organic solvents. This phenomenon was also observed through atomic force microscopy analysis (Figure S27). In acetone, FSOCA displayed a nanosheet-like morphology with a thickness of around 4 nm, whereas in water, it adopted a nanorod structure with a size of about 100 nm.

2.3 | Characterization of physicochemical properties

Water contact angle measurements (Figure 2(A–C)) revealed water contact angles of approximately 36°–39° for FSOCA and SOCA, and 92° for TPCA, indicating the hydrophilic nature of FSOCA and SOCA and the hydrophobic behavior for TPCA. Dynamic light scattering (Figure S28) revealed a relatively narrow size distribution of FSOCA and SOCA in water, whereas TPCA exhibited a broader size distribution. These findings confirmed that both SOCA and FSOCA exhibit significantly better hydrophilicity and dispersibility in water compared to TPCA.

A low exciton binding energy implies that photogenerated excitons are more easily separated, making it an important parameter for characterizing exciton separation in materials. We employed temperature-dependent photoluminescence to assess the exciton binding energy of these molecules (Figure 2(D–F)). By fitting the data using the Arrhenius equation, $I(T) = I_0/[1 + A\ \exp(-E_b/k_B \times T)]$, the calculated E_b for FSOCA, SOCA, and TPCA were 44, 14, and 210 meV, respectively. This means that FSOCA and SOCA exhibit weaker electron–hole pair interactions compared to TPCA, facilitating easier separation of excitons into carriers.[5]

Subsequently, spectroscopic analysis was conducted to investigate the photoelectric properties. Ultraviolet (UV)–vis reflectance spectra revealed absorption onsets at around 370 nm (SOCA), 450 nm (FSOCA), and 460 nm (TPCA) (Figure 2(H)). This indicates that compared to SOCA, FSOCA, and TPCA possess broader visible light absorption capabilities.[43] The charge transfer ability of these molecules was analyzed through electrochemical impedance spectroscopy. SOCA exhibited the highest conductivity, followed by FSOCA, with TPCA showing the lowest conductivity (Figure S29). Typically, improved conductivity promotes the efficient transport of

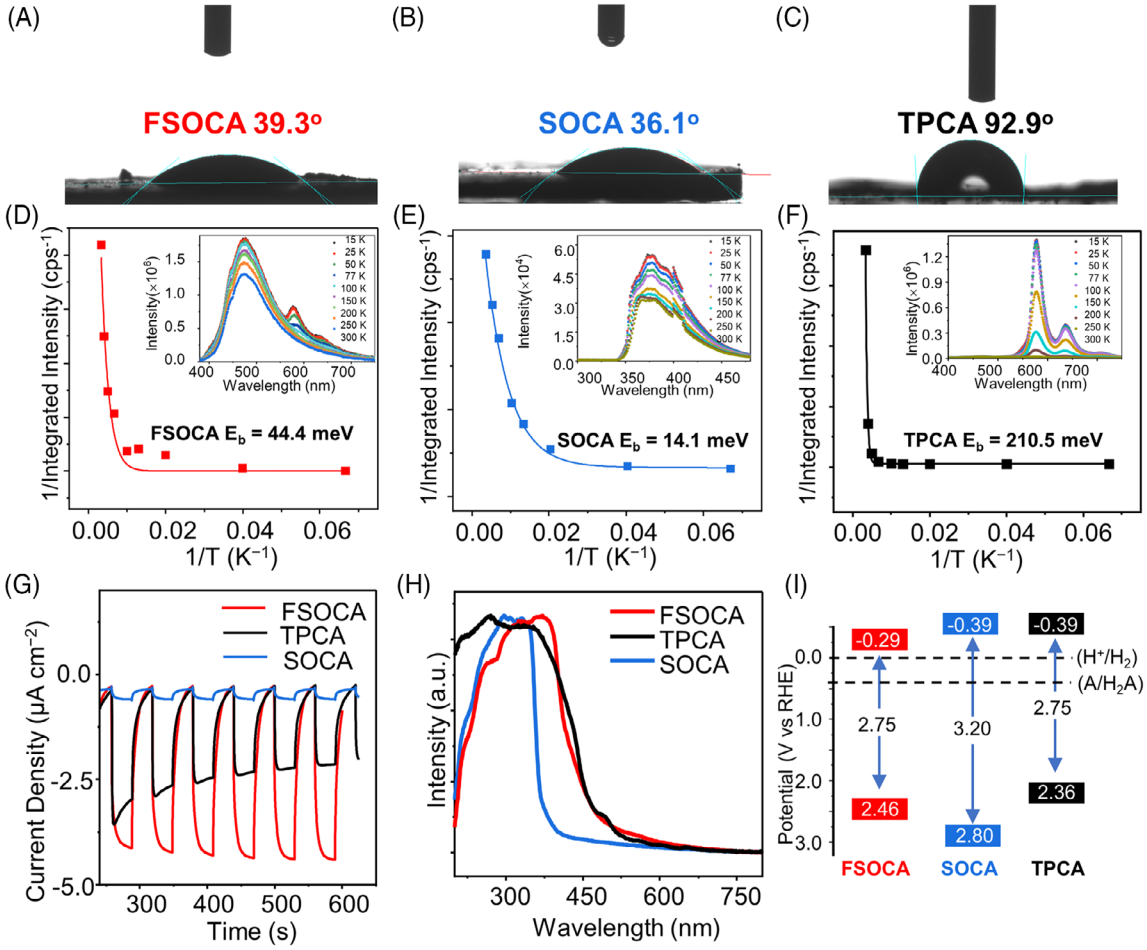

FIGURE 2 Water contact angle of (A) benzo [1,2-b:4,5-b′] bis [1] benzothiophene-3,9-dicarboxylic acid, 5,5,11,11-tetraoxide (FSOCA), (B) 5,5-dioxo-5H-dibenzo[b,d]thiophene-3,7-dicarboxylic acid (SOCA), and (C) [p-Terphenyl]−4,4″-dicarboxylic acid (TPCA). (D–F) The integrated Photoluminescence (PL) emission intensity as a function of temperature of FSOCA, SOCA, and TPCA in solid state. (G) The photocurrent curves. (H) The ultraviolet (UV)–vis absorption spectra. (I) Energy level of FSOCA, SOCA, and TPCA.

photogenerated excitons, thereby enhancing overall performance. However, under the utilized light source (>320 nm), SOCA displays a significantly narrower absorption spectrum, limited to wavelengths below 370 nm, whereas FSOCA has a broader absorption range extending to 450 nm. Consequently, this leads to a lower density of carriers generated for the SOCA than for the FSOCA, which is supported by the notably lower photocurrent density (Figure 2(G)).

The fluorescence spectra of FSOCA, SOCA, and TPCA exhibited maximum emission wavelengths of 478, 380, and 572 nm, and the average lifetimes were determined as 2.08, 0.56, and 6.68 ns, respectively (Figure S30).[11] We further tested the photoluminescence quantum yield to evaluate the separation and transport behavior of photo-generated charge carriers (Figures S31 and S32). The photoluminescence quantum efficiencies (φ_f) for FSOCA and TPCA are 6.0% and 44.5%, respectively. Considering that the photoluminescence quantum efficiency is the result of competition between fluorescence or phosphorescence radiation and other kinds of radiative or non-radiative transitions. A lower photoluminescence quantum efficiency (φ_f) of FSOCA may indicate faster electron transfer processes, while the photogenerated excitons of TPCA are more easily to recombine. The energy level structures of three molecules were analyzed using a combination of UV–vis reflectance spectroscopy and Mott–Schottky analysis (Figures S33 and 2(I)). Their energy level structures meet the energy requirements for HER and H_2O oxidation reactions.

2.4 | Photocatalytic experiments

Photocatalytic hydrogen evolution activity was evaluated on Labsolar-6A system (Beijing Perfectlight) using ascorbic acid (AA) as the sacrificial agent and platinum (Pt) as the co-catalyst. Under UV–vis light irradiation

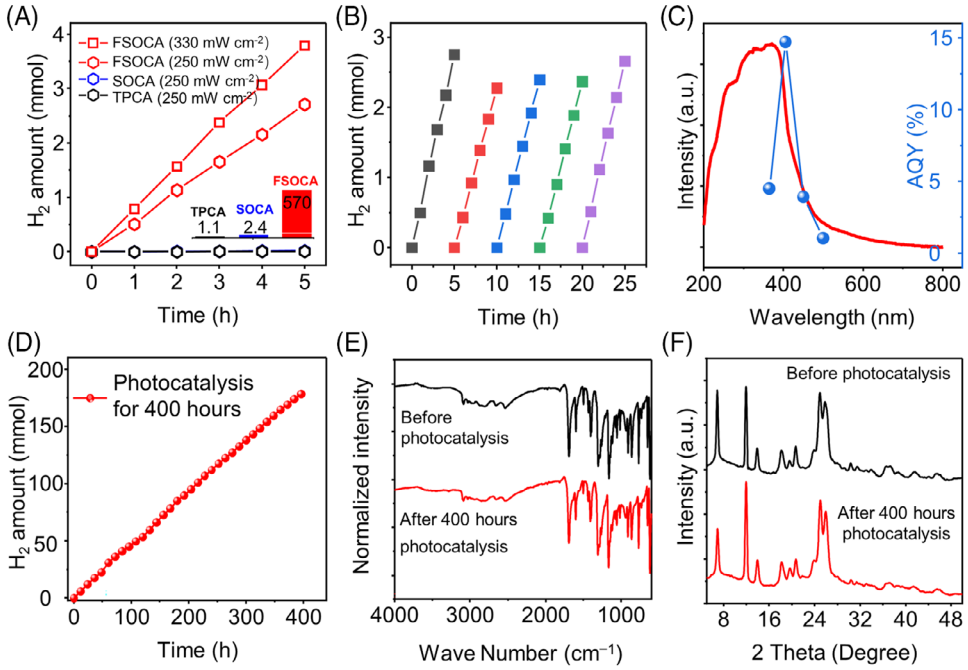

FIGURE 3 (A) Hydrogen evolution reaction (HER) performance of benzo [1,2-b:4,5-b′] bis [1] benzothiophene-3,9-dicarboxylic acid, 5,5,11,11-tetraoxide (FSOCA), 5,5-dioxo-5H-dibenzo[b,d]thiophene-3,7-dicarboxylic acid (SOCA), and [p-terphenyl]−4,4″-dicarboxylic acid (TPCA) ($\lambda \geq 320$ nm) (the inset is the performance comparison of TPCA, SOCA, and FSOCA; in μmol h^{-1}). (B) The cycle experiment of FSOCA. (C) The AQY of FSOCA. (D) The accumulated H_2 amount in a long-term (400 h) photocatalytic experiment of FSOCA. (E) Fourier transform infrared (FTIR) spectra of FSOCA after 400 h of photocatalysis experiment. (F) Powder X-ray diffraction (PXRD) pattern of FSOCA before and after 400 h of photocatalysis experiment.

($\lambda > 320$ nm, 250 mW cm^{-2}, Figure 3(A)), the average H_2 evolution of FSOCA was 570 μmol h^{-1} (57 mmol g^{-1} h^{-1}) (Figure S34). And the performance of FSOCA could reach up to 760 μmol h^{-1} (76 mmol g^{-1} h^{-1}) at $\lambda >$ 320 nm, 330 mW cm^{-2}. This ranks it among the top organic photocatalysts (Table S1). SOCA shows low performance (2.4 μmol h^{-1}, 240 μmol g^{-1} h^{-1}), which could be attributed to the restricted light absorption (Figure S35). The performance of TPCA was similarly low (1.1 μmol h^{-1}, 110 μmol g^{-1} h^{-1}). Moreover, the optimal Pt loading for FSOCA was determined to be approximately 0.43 wt% through analysis using inductively coupled plasma mass spectrometry (ICP-MS) (Figure S36 and Table S2). When using triethanolamine (TEOA) or methanol as sacrificial agents (Figure S37), the HER performance achieved is 6.0 mmol g^{-1} h^{-1} for TEOA and 1.54 mmol g^{-1} h^{-1} for methanol, both of which are significantly lower than that observed with ascorbic acid. This difference may stem from factors such as pH variations and discrepancies in redox potential. The wavelength-dependent apparent quantum yield (AQY) trend follows that of photoluminescence excitation spectroscopy, indicating wavelength-dependent hydrogen production (Figure S38). The AQY at 405 nm (±10 nm) is 14.7% (Figure 3(C) and Table S3).

FSOCA maintained its HER activity over five cycles (Figure 3(B)) and sustaining continuous hydrogen production for 24 h (Figure S39) without a notable decrease in activity, highlighting its excellent stability. FSOCA demonstrated continuous hydrogen evolution in extended photocatalytic experiments lasting 400 h (Figure 3(D)). FTIR and PXRD analyses were conducted to assess the chemical and crystalline structures of FSOCA after 400 h (Figure 3(E,F)). The FTIR spectra and PXRD patterns of FSOCA indicating the preservation of its structure. Furthermore, the morphology of FSOCA remained largely unchanged after the photocatalytic experiment (Figure S40). Transmission electron microscopy images revealed the presence of numerous Pt nanoparticles (ranging in size from 2.0 to 5.0 nm) on the surface of FSOCA following the photocatalysis experiments (Figure S41).

2.5 | Transient spectroscopy

Ultrafast transient absorption spectroscopy was employed to investigate the charge separation behavior. The negative signal ranging from 450 to 520 nm was attributed to the ground state bleach (GSB). In addition, positive signal from

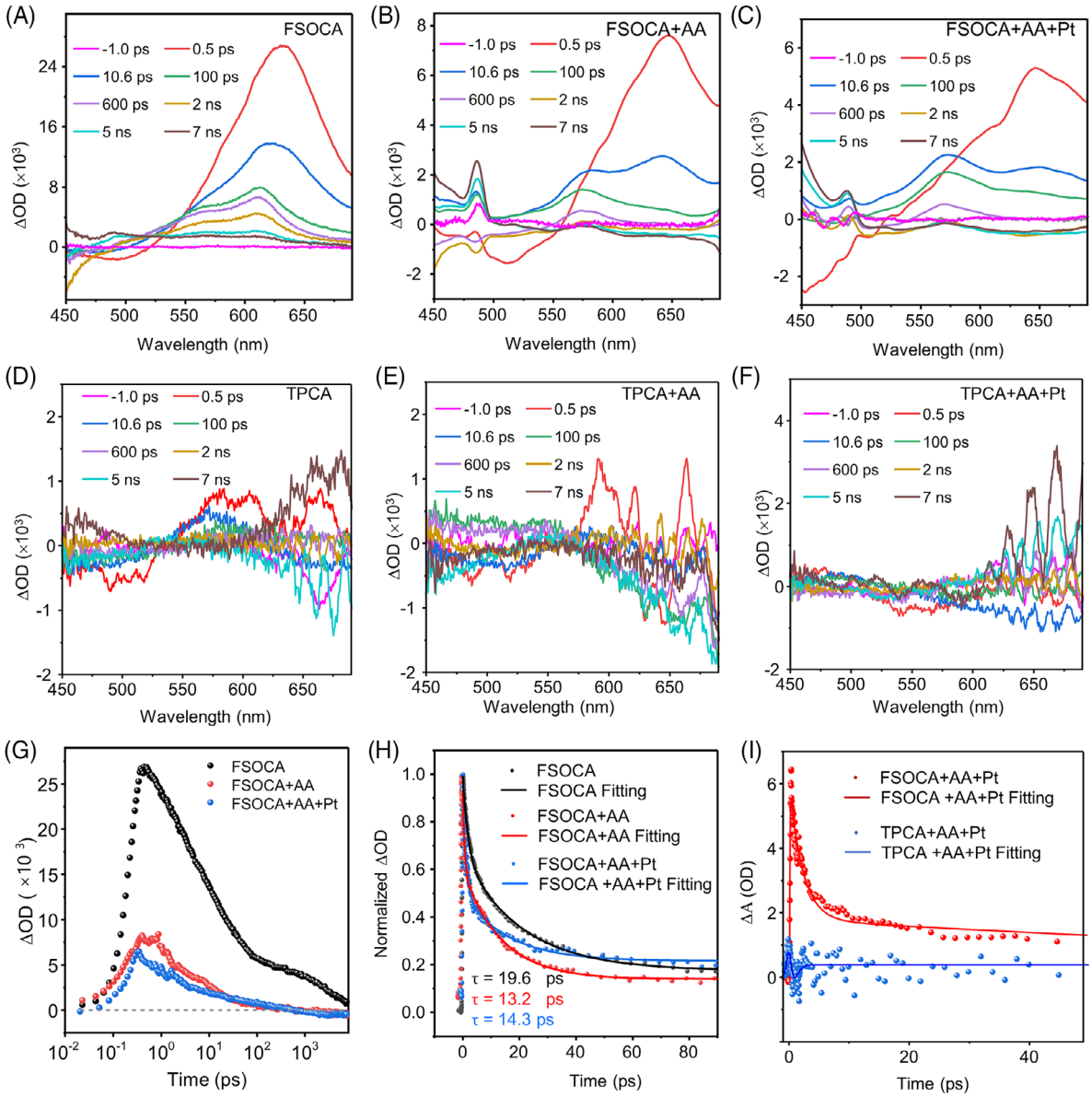

FIGURE 4 Transient absorption spectra obtained from suspensions. (A) Benzo [1,2-b:4,5-b′] bis [1] benzothiophene-3,9-dicarboxylic acid, 5,5,11,11-tetraoxide (FSOCA); (B) FSOCA + AA; (c) FSOCA + AA + Pt; (d) [p-terphenyl]−4,4″-dicarboxylic acid (TPCA); (E) TPCA + AA; (f) TPCA + AA + Pt. (G) Comparison of transient absorption decay kinetics at 650 nm for FSOCA, FSOCA + AA, and FSOCA + AA + Pt (λ_{ex} = 360 nm). (H) Transient kinetics probed at 650 nm for FSOCA, FSOCA + AA, FSOCA + AA + Pt, and (I) TPCA + AA+ Pt.

540 to 700 nm was attributed to trapped carriers because its formation corresponded to the decay of the GSB signal (Figures 4(A) and S42).[42,44,45] The trapped carriers were specifically identified as trapped holes based on their rapid decay with the introduce of the hole scavenger AA and AA + Pt (Figure 4(B,C,G)). In contrast, TPCA (Figure 4(D–F)) displayed minimal signal intensity between 450 and 700 nm following excitation at 360 nm, implying inefficient electron separation in aqueous systems.

The lifetimes of charge carriers were investigated through TA kinetics analysis of FSOCA and TPCA. In the case of FSOCA, both FSOCA + AA (13.2 ps) and FSOCA + AA + Pt (14.3 ps) exhibited shorter lifetimes compared to FSOCA alone (19.6 ps), indicating that the trapped holes were effectively quenched by AA (Figure 4(H) and Table S4). Conversely, both TPCA (1.1 ps) and TPCA + AA + Pt (0.46 ps) displayed shorter excited-state lifetimes than FSOCA + AA + Pt (14.3 ps) (Figures 4(I) and S43 and Table S4). This suggests that the introduction of sulfone groups in FSOCA results in a longer excited-state lifetime. Moreover, AA can rapidly capture the holes of FSOCA within several picoseconds, reducing the electron–hole recombination and enhancing FSOCA's activity for HER.

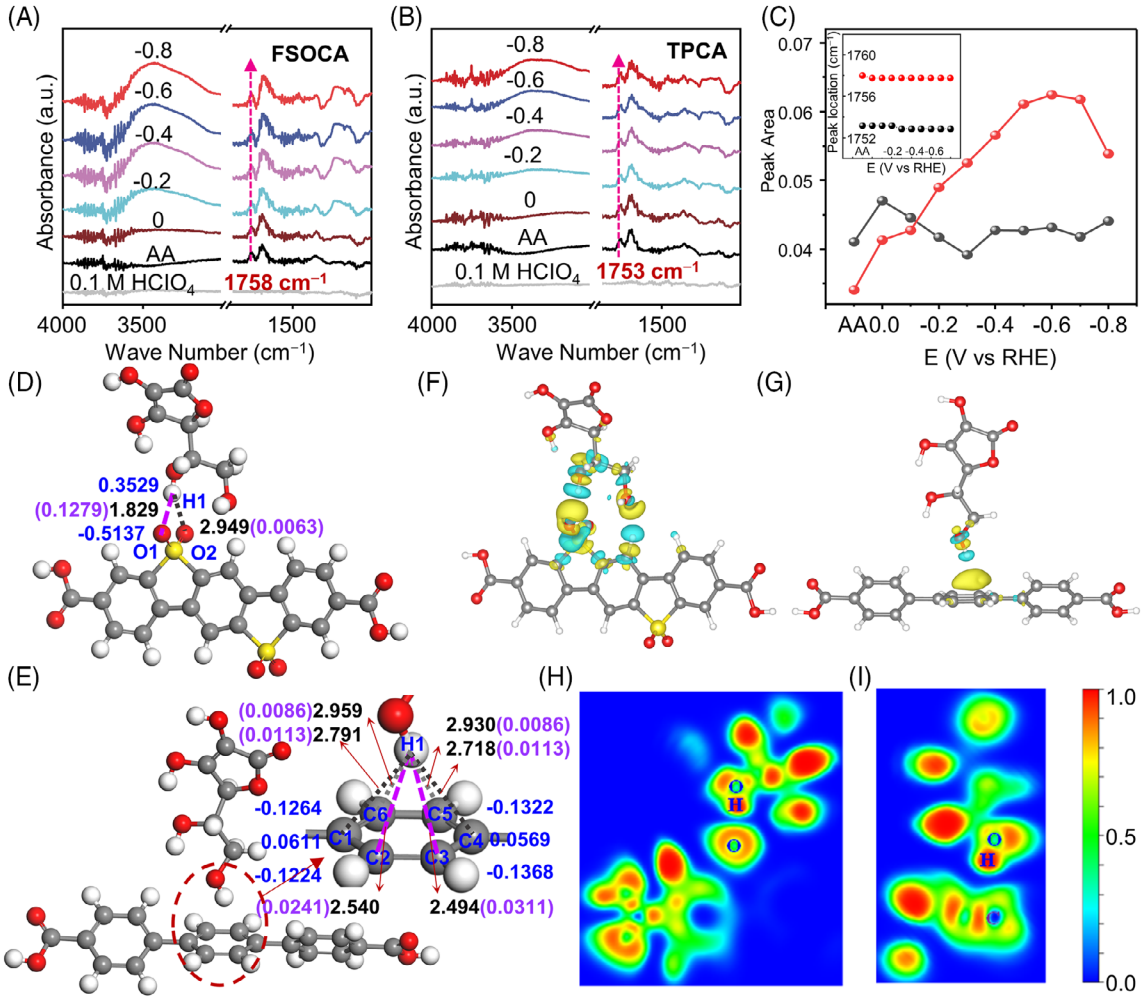

FIGURE 5 Surface-enhanced infrared absorption spectroscopy (SEIRA) spectra of (A) benzo [1,2-b:4,5-b′] bis [1] benzothiophene-3,9-dicarboxylic acid, 5,5,11,11-tetraoxide (FSOCA) and (B) [p-Terphenyl]−4,4″-dicarboxylic acid (TPCA). (C) The C═O peak area of ascorbic acid (AA) on FSOCA and TPCA with the change in potential; the inset is the C═O peak of AA on FSOCA and TPCA. (D) Computation of the bond length (black), net atomic charges (NACs) (blue), and bond orders (purple) of AA adsorbed on FSOCA and (E) TPCA. Atoms are colored by element: H (white), C (gray), O (red), and S (yellow). (F) Difference in the charge densities of AA adsorbed on FSOCA and (G) TPCA with an isosurface value of 0.001 e $Bohr^{-3}$, and the charge accumulation and depletion regions are colored in yellow and cyan. (H) Slab cut along O1–H1O and C3–H1O of ELF for AA adsorbed on FSOCA and (I) TPCA.

2.6 | The interaction between FSOCA and AA

To gain deeper insights into the impact of sulfone groups on the interaction and charge transfer processes between FSOCA and AA, we utilized in situ attenuated total reflection surface-enhanced infrared absorption spectroscopy (ATR-SEIRAS) to monitor the adsorbed species near the electrochemical interface. Before conducting the tests, background correction was performed using FSOCA and support as the electrochemical interfaces to mitigate interference from their signals. In the resulting spectra (Figure 5(A)), the positive peak observed at 1758 cm^{-1} is attributed to the C═O stretching mode in the ester group of AA. Conversely, when TPCA was used as the electrochemical interface (Figure 5(B)), the C═O stretching mode in the ester group of AA was observed at 1753 cm^{-1}. Additionally, the position of the C═O stretching mode remained unchanged with variations in applied potential for both FSOCA and TPCA (Figure 5(C), inset). However, when the potential decrease, the intensity increased for FSOCA at 1758 cm^{-1}, indicating specific adsorption of AA on FSOCA, and the intensity of the C═O stretching mode remained relatively constant with decreasing potential for TPCA (Figure 5(C)).[46] This suggests that AA is much more easily adsorbed on FSOCA than TPCA.

Theoretical calculations were employed to quantify the interaction strength between AA and the organic

photocatalysts (FSOCA and TPCA). According to computational analysis, the bond lengths of O1–H1 and O2–H1 were determined to be 1.829 and 2.949 Å, respectively, for AA adsorbed on FSOCA. This suggests a preference for AA to adsorb near the O atom rather than between two O atoms (Figure 5(D) and Table S5). This suggests the formation of hydrogen bonds between the hydroxyl groups in AA and the sulfonyl groups in FSOCA. In the case of AA adsorbed on TPCA, the shortest bond lengths were 2.494 and 2.540 Å for C3–H1 and C2–H1, respectively (Figure 5(E)). The adsorption energies of AA on FSOCA and TPCA were −0.40 and −0.19 eV, respectively. This indicates that the interaction between AA and FSOCA is stronger than that between AA and TPCA.

The charge density difference diagram reveals that the charge depletion regions on the H1 atom of AA–FSOCA (Figure 5(F)) are more extensive compared to those of AA–TPCA (Figure 5(G)). Furthermore, the blue regions between the O1 and H1 atoms of AA-FSOCA are lower than those between the C3 and H1 atoms in AA–TPCA. Overall, the electron localization function (ELF) value is relatively small for FSOCA (Figure 5(H,I)). The density-derived electrostatic and chemical (DDEC6) method was used to analyze hydrogen bonds. Quantitative atomic population analysis indicated hydrogen bond orders of 0.1279 (Figure 5(D), O1–H1) and 0.0241–0.0311 (Figure 5(E), C2–H1 and C3–H1) at the adsorption positions in the two materials. A higher bond order at O1–H1 corresponds to a greater desorption energy of the AA molecule. The net atomic charges of the hydrogen atom are measured at 0.3529 and 0.3293 |e|. This, along with the bond orders, provides evidence for the variance in charge density and the ELF diagram. These suggest that the hydrogen bonds exhibit a significant electrostatic character with a lesser covalent character. In conclusion, AA demonstrates greater ease of adsorption and stability on FSOCA compared to TPCA.

Taken together, various factors, including conjugated structure, crystallinity, and light absorption ability, play significant roles in influencing the efficacy of photoinduced proton reduction. The incorporation of sulfone groups enhances the delocalized range and rigidity of the molecular skeleton, resulting in lower exciton binding energy (44 meV for FSOCA compared with 210 meV for TPCA). Moreover, the rigid conjugated backbone enables FSOCA to attain higher ordered structures in contrast to TPCA. Reduction in exciton binding energy and highly crystalline structure facilitates the separation of photogenerated carriers, thereby reducing the recombination of carriers (evidenced by the excited-state lifetimes at 650 nm, which are 19.6 ps for FSOCA and 1.1 ps for TPCA). Additionally, the robust interaction between the sulfone group and sacrificial agents, such as AA, facilitates efficient electron transfer processes. In summary, the combination of a highly crystalline structure, low exciton binding energy, and strong interaction with sacrificial agents renders FSOCA a highly efficient and promising organic semiconductor-based photocatalyst for hydrogen evolution.

3 | CONCLUSION

Rationally designed sulfone-functionalized carboxyl acid photocatalysts (FSOCA) that offer the necessary chemistry (high crystallinity, easy-synthesized, and good stability) for photocatalytic HER have been reported. Incorporating the sulfonyl group serves to improve both the stability and hydrophilicity. As a result, the developed FSOCA achieved an HER rate of 76 mmol g^{-1} h^{-1}. Remarkably, FSOCA can maintain hydrogen production for 400 h. The interaction between FSOCA and the sacrificial agent was investigated through the utilization of in situ ATR-SEIRAS and computational calculations. AA exhibits greater ease of adsorption and enhanced stability on FSOCA compared to TPCA. Moreover, because of its high activity, photocatalytic stability, and ease of synthesis, FSOCA is promising material for other kinds of efficient photocatalytic applications or photo-electrocatalytic systems and challenging reactions, such as overall water splitting.

4 | EXPERIMENTAL

4.1 | Materials

SOCA (98%, Aladdin), P-terphenyl (99%, Aladdin), oxalyl chloride (98%, Aladdin), carbon disulfide (CS_2, 99.9%, Aladdin), aluminum chloride ($AlCl_3$, 99%, Aladdin), fuming sulfuric acid (20 wt.%, Sinopharm Chemical Reagent Co., Ltd.), sodium bicarbonate ($NaHCO_3$, 99.7%, Aladdin), hydrochloric acid (HCl, 36 wt. %, Sinopharm Chemical Reagent Co., Ltd.), sodium sulfate (Na_2SO_4, 97%, Aladdin), and AA (99.0%, Aladdin) were used. All the chemicals were used directly as received without further purification.

4.2 | Preparation of TPCA

First, 1.50 g of para-terphenyl (6.50 mmol) and 3.35 mL of oxalyl chloride were added into a 100 mL flask and 30 mL of carbon disulfide (CS_2) was added. Then, 1.475 g of aluminum chloride (11.06 mmol) was added under ice bath. After 1 h, 0.870 g of aluminum chloride (6.51 mmol) was added. The mixture was stirred at room temperature for 24 h. Then, the mixture was poured into crushed ice. The solid

was filtered after evaporating the carbon disulfide. The solid was washed by dilute hydrochloric acid and diethyl ether and then dried at 50°C to obtain a pale yellow solid. ^{1}H NMR (600 MHz, DMSO): δ 8.03 (d, 4H), 7.85 (d, 8H).

4.3 | Preparation of FSOCA

First, 0.5 g (1.57 mmol) of TPCA and 1.5 mL of fuming sulfuric acid (oleum H_2SO_4; 20% SO_3) were added in a 10 mL flask and refluxed at 120°C for 24 h. The mixture was added to 20 g of ice. A yellow precipitate was isolated via suction filtration, washed with H_2O and 1 M $NaHCO_3$ solution, and then isolated via suction filtration. The yellow cake was stirred in 1 M HCl for 1 h and isolated via suction filtration and drying at 50°C to get the final product. A yield of 0.60 g of FSOCA was obtained. ^{1}H NMR (600 MHz, DMSO): δ 8.94 (s, 2H), 8.31 (d, 2H), 8.23 (t, 4H).

ACKNOWLEDGMENTS

This work was supported by the National Natural Science Foundation of China (grant nos. 21975086, 22305087, and 52203259), the International S&T Cooperation Program of China (grant nos. 2018YFE0117300 and 22161142005), the Natural Science Foundation of Hubei Province (grant no. 2022CFB720). X. J. Y. and X. Y. acknowledge the support from the Huazhong University of Science and Technology (HUST) Academic Frontier Youth Team (grant no. 2019QYTD11). L. M. Y. and B. Y. S. gratefully acknowledge the National Natural Science Foundation of China (21873032, 22073033, 21673087, and 21903032), the startup fund from HUST (2006013118 and 3004013105), the Fundamental Research Funds for the Central Universities (2019kfyRCPY116), and the Innovation and Talent Recruitment Base of New Energy Chemistry and Device (B21003). We thank the Analysis and Testing Center, HUST, for characterization of materials. We greatly appreciate associate Prof. Songhua Cai from the Hong Kong Polytechnic University for TEM testing and analysis. The computing work in this paper is supported by the public service platform of high performance computing by network and computing center of HUST.

CONFLICT OF INTEREST STATEMENT

The authors declare no conflict of interest.

DATA AVAILABILITY STATEMENT

Cambridge Crystallographic Data Centre (CCDC) 2251963 and 892248 contains the supplementary crystallographic data for this paper. These data can be obtained free of charge from the CCDC via www.ccdc.cam.ac.uk/data_request/cif

ORCID

Bien Tan https://orcid.org/0000-0001-7181-347X

REFERENCES

1. Zhao D, Wang Y, Dong C-L, et al. Boron-doped nitrogen-deficient carbon nitride-based Z-scheme heterostructures for photocatalytic overall water splitting. *Nat Energy*. 2021;6(4):388-397.
2. Nishiyama H, Yamada T, Nakabayashi M, et al. Photocatalytic solar hydrogen production from water on a 100-m^2 scale. *Nature*. 2021;598(7880):304-307.
3. Guo Y, Qixin ZS, Nan J, Shi W, Cui F, Zhu Y. Perylenetetracarboxylic acid nanosheets with internal electric fields and anisotropic charge migration for photocatalytic hydrogen evolution. *Nat Commun*. 2022;13(1):2067.
4. Li C, Liu J, Li H, Wu K, Wang J, Yang Q. Covalent organic frameworks with high quantum efficiency in sacrificial photocatalytic hydrogen evolution. *Nat Commun*. 2022;13(1):2357.
5. Lan Z, Zhang G, Chen X, et al. Reducing the exciton binding energy of donor–acceptor-based conjugated polymers to promote charge-induced reactions. *Angew Chem Int Ed*. 2019;58(30):10236-10240.
6. Habibi-Yangjeh A, Pournemati K. A review on emerging homojunction photocatalysts with impressive performances for wastewater detoxification. *Crit Rev Environ Sci Tech*. 2024;54(4):290-320.
7. Seifikar F, Habibi-Yangjeh A. Floating photocatalysts as promising materials for environmental detoxification and energy production: a review. *Chemosphere*. 2024;355:141686.
8. Zhao C, Chen Z, Shi R, Yang X, Zhang T. Recent advances in conjugated polymers for visible-light-driven water splitting. *Adv Mater*. 2020;32(28):1907296.
9. Wang X, Maeda K, Thomas A, et al. A metal-free polymeric photocatalyst for hydrogen production from water under visible light. *Nat Mater*. 2009;8(1):76-80.
10. Hemmati-Eslamlu P, Habibi-Yangjeh A. A review on impressive Z- and S-scheme photocatalysts composed of g-C_3N_4 for detoxification of antibiotics. *FlatChem*. 2024;43:100597.
11. Lv Y, Ma D, Song K, et al. Graphitic carbon nitride decorated with C–N compounds broken by *s*-triazine unit as homojunction for photocatalytic H_2 evolution. *J Mater Chem A*. 2023;11(2):800-808.
12. Ma D, Zhang Z, Zou Y, Chen J, Shi J. The progress of g-C_3N_4 in photocatalytic H_2 evolution: from fabrication to modification. *Coordin Chem Rev*. 2024;500:215489.
13. Yu H, Shi R, Zhao Y, et al. Alkali-assisted synthesis of nitrogen deficient graphitic carbon nitride with tunable band structures for efficient visible-light-driven hydrogen evolution. *Adv Mater*. 2017;29(16):1605148.
14. Yanagida S, Kabumoto A, Mizumoto K, Pac C, Yoshino K. Poly(p-phenylene)-catalysed photoreduction of water to hydrogen. *Chem Commun*. 1985;8(8):474-475.
15. Sachs M, Sprick RS, Pearce D, et al. Understanding structure-activity relationships in linear polymer photocatalysts for hydrogen evolution. *Nat Commun*. 2018;9(1):4968.
16. Sprick RS, Jiang J-X, Bonillio B, et al. Tunable organic photocatalysts for visible-light-driven hydrogen evolution. *J Am Chem Soc*. 2015;137(9):3265-3270.

17. Yang C, Ma BC, Zhang L, et al. Molecular engineering of conjugated polybenzothiadiazoles for enhanced hydrogen production by photosynthesis. *Angew Chem Int Ed*. 2016;55(32):9202-9206.
18. Li L, Cai Z, Wu Q, et al. Rational design of porous conjugated polymers and roles of residual palladium for photocatalytic hydrogen production. *J Am Chem Soc*. 2016;138(24):7681-7686.
19. Wang X, Chen L, Chong SY, et al. Sulfone-containing covalent organic frameworks for photocatalytic hydrogen evolution from water. *Nat Chem*. 2018;10(12):1180-1189.
20. Wang H, Wang H, Wang Z, et al. Covalent organic framework photocatalysts: structures and applications. *Chem Soc Rev*. 2020;49(12):4135-4165.
21. Wang H, Zeng Z, Xu P, et al. Recent progress in covalent organic framework thin films: fabrications, applications and perspectives. *Chem Soc Rev*. 2019;48(2):488-516.
22. Hu X, Zhan Z, Zhang J, Hussain I, Tan B. Immobilized covalent triazine frameworks films as effective photocatalysts for hydrogen evolution reaction. *Nat Commun*. 2021;12(1):6596.
23. Liu M, Huang Q, Wang S, et al. Crystalline covalent triazine frameworks by in situ oxidation of alcohols to aldehyde monomers. *Angew Chem Int Ed*. 2018;57(37):11968-11972.
24. Wang K, Yang L, Wang X, et al. Covalent triazine frameworks via a low-temperature polycondensation approach. *Angew Chem Int Ed*. 2017;56(45):14149-14153.
25. Sun T, Liang Y, Xu Y. Rapid, ordered polymerization of crystalline semiconducting covalent triazine frameworks. *Angew Chem Int Ed*. 2022;61(4):e202113926.
26. Lin L, Lin Z, Zhang J, Cai X. Molecular-level insights on the reactive facet of carbon nitride single crystals photocatalysing overall water splitting. *Nat Catal*. 2020;3(8):649-655.
27. Algara-Siller G, Severin N, Chong SY, et al. Triazine-based graphitic carbon nitride: a two-dimensional semiconductor. *Angew Chem Int Ed*. 2014;53(29):7450-7455.
28. Lin L, Wang C, Ren W, Ou H, Zhang Y, Wang X. Photocatalytic overall water splitting by conjugated semiconductors with crystalline poly(triazine imide) frameworks. *Chem Sci*. 2017;8(8):5506-5511.
29. Aitchison CM, Kane CM, McMahon DP, et al. Photocatalytic proton reduction by a computationally identified, molecular hydrogen-bonded framework. *J Mater Chem A*. 2020;8(15):7158-7170.
30. Zhu Y, Zhang Z, Si W, et al. Organic photovoltaic catalyst with extended exciton diffusion for high-performance solar hydrogen evolution. *J Am Chem Soc*. 2022;144(28):12747-12755.
31. Zhang Z, Si W, Wu B, et al. Two-dimensional polycyclic photovoltaic molecule with low trap density for high-performance photocatalytic hydrogen evolution. *Angew Chem Int Ed*. 2022;61(10):e202114234.
32. Weingarten AS, Kazantsev RV, Palmer LC, et al. Self-assembling hydrogel scaffolds for photocatalytic hydrogen production. *Nat Chem*. 2014;6(11):964-970.
33. Dannenhoffer A, Sai H, Harutyunyan B, et al. Growth of extra-large chromophore supramolecular polymers for enhanced hydrogen production. *Nano Lett*. 2021;21(9):3745-3752.
34. Weingarten A, Dannenhoffer A, Kazantsev R, Sai H, Huang D, Stupp S. Chromophore dipole directs morphology and photocatalytic hydrogen generation. *J Am Chem Soc*. 2018;140(15):4965-4968.
35. Kong K, Zhang S, Chu Y, et al. A self-assembled perylene diimide nanobelt for efficient visible-light-driven photocatalytic H_2 evolution. *Chem Commun*. 2019;55(56):8090-8093.
36. Jing J, Yang J, Zhang Z, Zhu Y. Supramolecular zinc porphyrin photocatalyst with strong reduction ability and robust built-in electric field for highly efficient hydrogen production. *Adv Energy Mater*. 2021;11(29):2101392.
37. Zhang N, Wang L, Wang H, et al. Self-assembled one-dimensional porphyrin nanostructures with enhanced photocatalytic hydrogen generation. *Nano Lett*. 2018;18(1):560-566.
38. Zhang Z, Zhu Y, Chen X, Zhang H, Wang J. A full-spectrum metal-free porphyrin supramolecular photocatalyst for dual functions of highly efficient hydrogen and oxygen evolution. *Adv Mater*. 2019;31(7):1806626.
39. Zhang G, Yang X, Li Y, Zhang P, Mi H. Donor–acceptor cyanocarbazole-based supramolecular photocatalysts for visible-light-driven H_2 production. *ChemSusChem*. 2019;12(23):5070-5074.
40. Yang H, Li C, Liu T, et al. Packing-induced selectivity switching in molecular nanoparticle photocatalysts for hydrogen and hydrogen peroxide production. *Nat Nanotechnol*. 2023;18(3):307-315.
41. Eberhart MS, Wang D, Sampaio RN, et al. Water photo-oxidation initiated by surface-bound organic chromophores. *J Am Chem Soc*. 2017;139(45):16248-16255.
42. Clarke T, Durrant J. Charge photogeneration in organic solar cells. *Chem Rev*. 2010;110(11):6736-6767.
43. Ma Y, Fang H, Chen R, et al. 2D-MOF/2D-MOF heterojunctions with strong hetero-interface interaction for enhanced photocatalytic hydrogen evolution. *Rare Met*. 2023;42(12):3993-4004.
44. Hillman SAJ, Sprick RS, Pearce D, et al. Why do sulfone-containing polymer photocatalysts work so well for sacrificial hydrogen evolution from water? *J Am Chem Soc*. 2022;144(42):19382-19395.
45. Kosco J, Gonzalez-Carrero S, Howells CT, et al. Generation of long-lived charges in organic semiconductor heterojunction nanoparticles for efficient photocatalytic hydrogen evolution. *Nat Energy*. 2022;7(4):340-s351.
46. Yang X, Nash J, Oliveira N, Yan Y, Xu B. Understanding the pH dependence of underpotential deposited hydrogen on platinum. *Angew Chem Int Ed*. 2019;58(49):17718-17723.

SUPPORTING INFORMATION

Additional supporting information can be found online in the Supporting Information section at the end of this article.

How to cite this article: Hu X, Yang X, Song B, et al. Sulfone-functionalized stable molecular single crystals for photocatalytic hydrogen evolution. *SusMat*. 2024;4:e220. https://doi.org/10.1002/sus2.220